

Limit Analysis and Stability Charts for 3D Slope Failures

Radoslaw L. Michalowski, F.ASCE¹

Abstract: The kinematic approach of limit analysis is explored in three-dimensional (3D) stability analysis of slopes. A formal derivation is first shown indicating that, in a general case, the approach yields an upper bound to the critical height of the slope or an upper bound on the safety factor. A 3D failure mechanism is used to produce stability charts for slopes. The slope safety factor can be read from the charts without the need for iterations. While two-dimensional (2D) analyses of uniform slopes lead to lower safety factors than 3D analyses do, a 3D calculation is justified in cases where the width of the collapse mechanism has physical limitations, for instance, in the case of excavation slopes, or when the analysis is carried out to back-calculate the properties of the soil from 3D failure case histories. Also, a 3D failure can be triggered by a load on a portion of the surface area of the slope. Calculations indicate that for the 3D safety factor of the loaded slope to become lower than the 2D factor for the same slope (but with a load-free surface), the load has to be very significant and equal to the weight of a soil column of the order 10^{-1} of the slope height.

DOI: 10.1061/(ASCE)GT.1943-5606.0000251

CE Database subject headings: Slope stability; Limit analysis; Landslides; Plasticity; Failures; Three-dimensional analysis.

Author keywords: Slope stability; Limit analysis; Landslides; Plasticity; Failure; Three-dimensional analysis; Loaded slopes.

Introduction

Three-dimensional (3D) analyses of slope stability are not often used in practical applications as they are more elaborate than plane-strain analyses, and no convenient methods have been developed for performing such analyses. A two-dimensional (2D) (plane strain) analysis also can be regarded as conservative in cases where 3D failure should be expected, and it is often preferred in design (Cornforth 2005). There are cases, however, where a 3D failure analysis is justified, for instance, in back calculations of soil properties for slopes that have failed, or when the width of the failure mechanism is well defined, for instance, in excavation slopes.

An extensive review of the literature regarding stability analysis of slopes was presented by Duncan (1996). Some of the newer literature, focused particularly on the 3D analyses, can be found in a more recent paper by Griffiths and Marquez (2007). Of particular interest in this article is the kinematic approach of limit analysis with application to 3D failures. An early application of this method was shown by Drucker and Prager (1952), who considered a slope failing under plane-strain conditions. A simple 3D collapse with a single block was analyzed by Drescher (1983) in the context of collapsing material in storage containers. A multi-block 3D translational mechanism for slopes was considered in Michalowski (1989), whereas a rotational mechanism was constructed by de Buhan and Garnier (1998). Several authors used an approach to 3D analysis that is equivalent to limit analysis, but based on global equilibrium of forces or moments (Baligh and

Azzouz 1975; Leshchinsky and Baker 1986; Gens et al. 1988); many of those relate only to the limit states under undrained conditions.

In his limit analysis of a 2D slope collapse, Chen (1975) noticed that it is a rotational mechanism (not translational) that leads to the most critical case. This motivated Michalowski and Drescher (2009) to construct a 3D rotational mechanism for slope collapse, and this mechanism is adopted here to develop stability charts for slopes failing in a 3D fashion. These charts allow estimation of the factor of safety against a 3D failure without the need for an iterative procedure. First, the use of kinematic limit analysis is considered to obtain a rigorous bound on the safety factor, followed by a discussion of applicability of the analysis to soils described by the Mohr-Coulomb yield condition. Next, a 3D mechanism of failure is described, the numerical procedure is briefly explained, and the stability charts are developed. The concept of a "significant load" is introduced to define a load distributed on some portion of the slope surface that would produce a 3D safety factor that is lower than one from a 2D analysis. The paper is concluded with some final remarks.

Limit Analysis in Slope Stability

Most engineering analyses of slope stability seek the factor of safety, which is a traditional measure of the safety margin. Hence, these analyses are not typical limit state problems where the magnitude of the load is sought, causing the structure to fail. The solution to a stability problem must be dependent on the geometry of the slope (height, inclination angle, and the width of the mechanism B , if 3D analysis is carried out) and the strength properties of the soil (consider first the undrained shear strength c_u), as well as the soil weight (measured by its unit weight γ). Introducing a dimensionless group $\gamma H/c_u$, the number of independent parameters in the analysis can be reduced by two. The limit value of $\gamma H/c_u$ is often called the *dimensionless critical height*. The ratio of the critical rate of $\gamma H/c_u$ to its true value for an existing

¹Professor, Dept. of Civil and Environmental Engineering, Univ. of Michigan, 2340 G. G. Brown Bldg., Ann Arbor, MI 48109. E-mail: rlmich@umich.edu

Note. This manuscript was submitted on June 4, 2009; approved on September 15, 2009; published online on March 15, 2010. Discussion period open until September 1, 2010; separate discussions must be submitted for individual papers. This paper is part of the *Journal of Geotechnical and Geoenvironmental Engineering*, Vol. 136, No. 4, April 1, 2010. ©ASCE, ISSN 1090-0241/2010/4-583-593/\$25.00.

slope is a measure of the slope safety and, for the soil characterized by the undrained shear strength, it is identical to the traditional factor of safety.

The notion of a critical height in the context of limit analysis appears in an early paper of Drucker and Prager (1952); they indicate, though only for a special case, that the kinematic approach of limit analysis leads to an upper bound on the true critical height. Intuitively, the *factor of safety* following from the kinematic approach is also an upper-bound estimate (e.g., Michalowski 1989); a more rigorous justification of this statement is given below.

In a typical slope stability analysis the only load considered is that of the soil weight. This load is given in terms of the unit weight γ , and the limit analysis problem can be stated in the following manner: find the magnitude of unit weight γ that will cause the slope of given geometry to fail. Considering that the slope also may be loaded with a given distributed load (traction) p_i on boundary S , the principle of virtual work written for the true (but unknown) stresses field σ_{ij} produced by the soil weight γ , on the kinematically admissible mechanism with strain rates $\dot{\epsilon}_{ij}^k$, takes the form

$$\int_V \sigma_{ij} \dot{\epsilon}_{ij}^k dV = \gamma \int_V n_i v_i^k dV + \int_S p_i v_i^k dS \quad (1)$$

where the unit weight vector γ_i was written as the product of its magnitude γ and the unit vector n_i in the direction of gravity. V is the volume of the mechanism, and S is its surface; superscript k denotes the kinematically admissible velocity and strain rate fields. An energy balance equation for stresses and loads associated with the same kinematically admissible mechanism can be written as

$$\int_V \sigma_{ij}^k \dot{\epsilon}_{ij}^k dV = \gamma^k \int_V n_i v_i^k dV + \int_S p_i v_i^k dS \quad (2)$$

where stress σ_{ij}^k is associated with the admissible kinematics $\dot{\epsilon}_{ij}^k$, but it is not necessarily in equilibrium [therefore, balance Eq. (2) is not the principle of virtual work]. Subtracting Eq. (1) from Eq. (2) we have

$$\int_V (\sigma_{ij}^k - \sigma_{ij}) \dot{\epsilon}_{ij}^k dV = (\gamma^k - \gamma) \int_V n_i v_i^k dV \quad (3)$$

For the flow rule associated with a convex yield condition, the integral on the left-hand side of Eq. (3) is never negative, whereas the integral on the right-hand side is always positive, hence

$$\gamma^k \geq \gamma \quad (4)$$

Therefore, if the balance Eq. (2) is used to calculate an estimate of the unit weight causing failure, γ^k , this estimate will be not less than the true value of γ causing the slope to collapse. Because $\gamma H/c_u$ is a dimensionless group in the problem, the inequality in Eq. (4) can be multiplied by the true value of H/c_u , to yield

$$\frac{\gamma^k H}{c_u} = \left(\frac{\gamma H}{c_u} \right)^k \geq \frac{\gamma H}{c_u} \quad (5)$$

So it becomes evident that $\gamma^k H/c_u$ calculated from the kinematic approach is an upper estimate of its true critical value. This conclusion was obtained earlier for special cases (vertical cut, uniform slopes) directly from the kinematic theorem of limit analysis (Drucker and Prager 1952; Salençon 1990). However, the result

in Eq. (5) is more general, as it has been derived without reference to a specific example.

Alternatively, the kinematic approach yields the lower estimate of the stability factor $c_u/\gamma H$ (introduced earlier by Taylor 1937)

$$\left(\frac{c_u}{\gamma H} \right)^k \leq \frac{c_u}{\gamma H} \quad (6)$$

Traditional slope analyses seek the safety factor, typically defined as the ratio of the shear strength of the soil to that necessary to maintain limit equilibrium; for undrained shear strength

$$F = \frac{c_u}{c_{ud}} \quad (7)$$

where c_{ud} =undrained shear strength needed to maintain limit equilibrium. The kinematic limit analysis leads to $(\gamma H/c_u)^k$, which is an upper estimate of true $\gamma H/c_u$ at failure, as indicated in inequality (5). Given true γH for a slope, one can write

$$\left(\frac{\gamma H}{c_u} \right)^k = \frac{\gamma H}{c_u^k} \quad (8)$$

where c_u^k =lower estimate of the undrained shear strength c_u necessary to keep the slope stable. Now, considering Eqs. (5) and (8), and replacing c_u^k with c_u/F^k and c_u with c_u/F , one obtains

$$F^k \frac{\gamma H}{c_u} \geq F \frac{\gamma H}{c_u} \quad \text{or} \quad F^k \geq F \quad (9)$$

Hence, kinematic analysis leads to the upper-bound estimate on the factor of safety as defined in Eq. (7). This conclusion holds true, of course, for both the 2D and 3D limit analysis calculations.

It might be of interest to note that the conclusion above also holds for traditional limit equilibrium considerations, for as long as the failure pattern is kinematically admissible, and no arbitrary assumption regarding distribution of forces is used. The proof of this equivalency was included in Michalowski (1989), and a more comprehensive consideration of the duality of this approach can be found in Salençon (1990).

3D versus 2D Safety Analyses

It is commonly accepted that 3D analyses yield safety factors for slopes that are not lower than those from plane-strain (2D) analyses. This statement is supported by direct comparison of analytical results, and by intuition (2D analysis is less restrictive). Some effort was made earlier by Cavounidis (1987) to justify this statement. He concluded that the occasional result of a 3D safety factor being lower than that from a 2D analysis is due to simplifying assumptions often made in the former. Here, we offer a more formal justification for the statement that a 2D safety factor for a uniform slope cannot be larger than that from a 3D analysis.

Consider a soil slope limited to some width B by, for instance, rough walls, or a rock formation. Collapse of such a slope will be three dimensional, minimizing the effect of the rough constraints. Now, consider the second slope, similar to the first one, but with smooth vertical planes at the two ends. The failure mechanism will now be attracted to these planes as the sliding on the smooth planes requires no energy to be expanded. This will result in a plane-strain mechanism of failure, with all velocity vectors parallel to the smooth planes. The difference between the two slopes is in the smooth planes that can be considered as weak planes (zero strength), or zones of a weaker material. We now invoke the corollary theorem (Drucker et al. 1952) stating that: "if the yield surface of one material contains that of a second material, the first

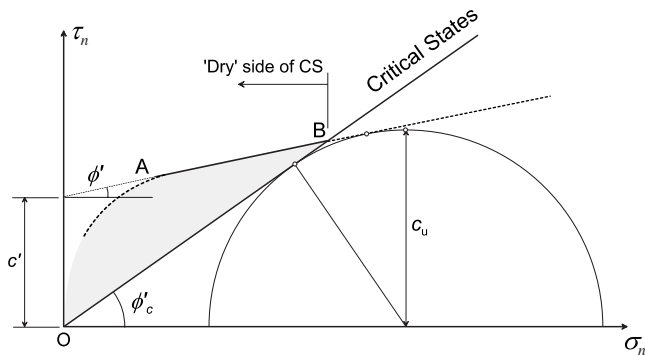


Fig. 1. Interpretation of the yield condition used in limit analysis

material will be said to have *higher yield strength* than the second,” and another consequence of the theorems: a decrease in material strength of a structure will not produce an increase in the limit load. The yield surfaces of the soil in the two slopes coincide, except along the weak planes, where the yield surface of the soil in the first slope contains the second one. Consequently, the limit load on the first slope cannot be lower than that on the second slope, or, the safety factor for the first one will not be lower than that for the second one. Because the smooth planes in the second slope favor the plane mechanism of failure, the safety factor from the 2D analysis cannot be higher than that from a 3D analysis.

Applicability of Limit Analysis Calculations to Slopes

Limit analysis is applicable to soils whose strength is described with a convex yield condition and whose deformation is governed by the normality flow rule. Soils failing in undrained conditions can be characterized by their undrained shear strength c_u and incompressible plastic deformation, thus satisfying the requirements of limit analysis applicability. Overconsolidated clays and silts failing in a drained process, however, exhibit some frictional component of the strength, and their failure envelope is typically represented by the Mohr-Coulomb yield condition with internal friction angle ϕ' and cohesion intercept c' . In the context of critical states such an envelope is located on the “dry side,” and is the locus of the soil peak strength. This is illustrated in Fig. 1. It is considered here that the strength of the soil is described by the line passing through Points A and B in Fig. 1, and the computational results will be presented in term of ϕ' and c' (for brevity, the *prime* will be omitted in further description, i.e., $\phi = \phi'$ and $c = c'$).

It is reasonable to ask whether the strength due to “cohesiveness” of fine-grained soils (the shaded area in Fig. 1) should be accounted for in engineering design. This cohesiveness is often interpreted as having an origin in bonding between particles or interlocking. Many short-term stability considerations can rely on the peak strength, whereas the peak strength in long-term stability analysis can only be relied on if the cohesiveness in the soil is maintained, and the peak strength is never reached. For instance, a footing founded on an overconsolidated clay can usually take advantage of the peak strength, but a vertical cut in clay, even though stable at first, will collapse some time after its excavation. The peak strength is used in limit analysis only to calculate the limit load, but the applied load on the structure is to be main-

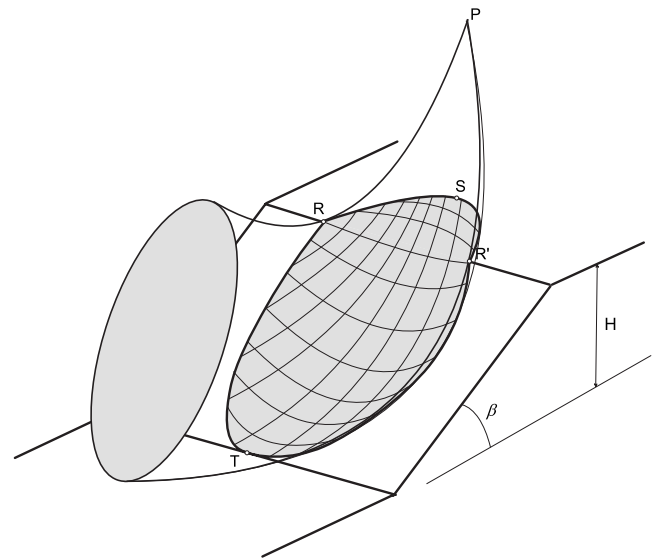


Fig. 2. Schematic of the 3D failure mechanism

tained well below the limit load. An argument for presenting the charts based on the Mohr-Coulomb yield condition is also in existing natural slopes with inclination exceeding the limit set by the critical states, indicating the contribution of soil cohesiveness to strength. This is not to say that the Mohr-Coulomb yield condition with a cohesion intercept can be used universally for all slopes; for instance, caution needs to be exercised if slopes are likely to be submerged.

3D Rotational Failure Pattern of Slopes

3D mechanisms for dilatant soils are difficult to construct because of the increase in volume that needs to be accommodated as the material shears. An example of a 3D multiblock translational mechanism was shown earlier by Michalowski (1989). It was pointed out by Chen (1975) that, in plane-strain analysis, a rotational failure mechanism yields the least (best) estimate of the critical height $\gamma H/c$. More recently, a 3D rotational mechanism was constructed by Michalowski and Drescher (2009), with the failure surface being a section of a curvilinear cone (a “horn”). A surface of this kind was used earlier in consideration of bearing capacity under square and rectangular footings (Michalowski 2001). This mechanism is adopted here, and it is shown schematically in Fig. 2. A more comprehensive description and discussion of this mechanism can be found in Michalowski and Drescher (2009); here, the main features of the mechanism are described, and the equations are reproduced for the reader to be able to recreate the results.

The purpose of the analysis is to develop stability charts for 3D slope failures for a practical range of geometrical and material parameters, and present them in such a manner so that the safety factor can be obtained without the need for iterations.

Frictional Soils

The curvilinear cone surface with apex at P, Fig. 2, intersects the top surface of the slope along trace RSR', and its cross section with the sloping surface is marked with the curve RTR'. The surface over which the soil slides has a spoonlike shape. During failure, the soil contained in the volume determined by the slope

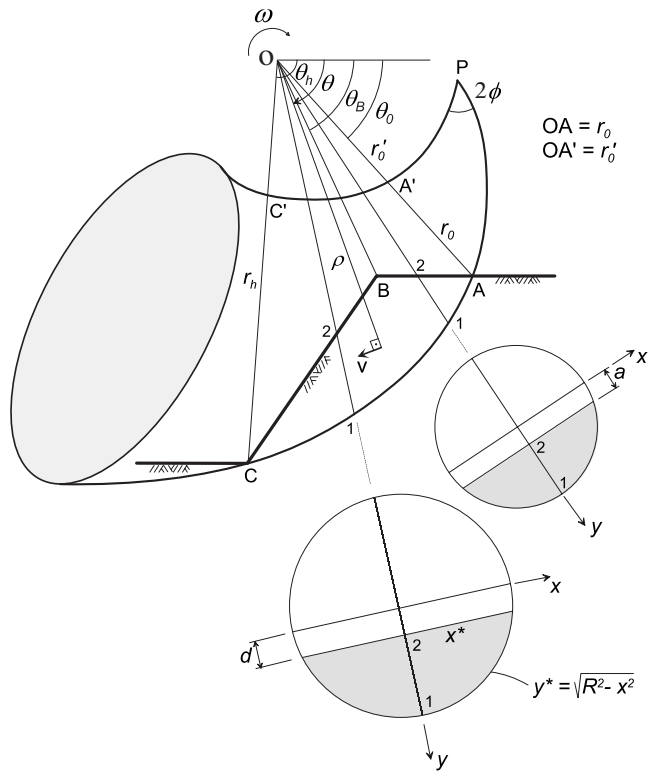


Fig. 3. 3D mechanism generated by rotation of a circle with variable diameter [after Michalowski and Drescher (2009)]

contour and the spoonlike surface undergoes rotation about an axis parallel to the crest line RR' . Kinematical admissibility requires that along the entire sliding surface the vector of velocity of the rotating soil be inclined at angle ϕ to that surface; this assures that the dilatancy (volume increase) of the shearing soil is accommodated by the mechanism. This dilatancy is the direct consequence of the Mohr-Coulomb yield condition (line AB in Fig. 1) and the normality flow rule. To satisfy this admissibility requirement the apex angle of the curvilinear cone in Fig. 2 needs to be equal to 2ϕ .

The cross section through the symmetry plane of the mechanism is illustrated in Fig. 3. During failure, the soil mass rotates about axis passing through Point O . The cross sections of the horn with planes intersecting the axis of rotation are circular. Two such cross sections are illustrated in Fig. 3. The trace of the cone on the plane of the figure is marked by two log-spirals: PAC and $PA'C'$, described by equations

$$r = r_0 e^{(\theta - \theta_0) \tan \phi} \quad (10)$$

and

$$r' = r'_0 e^{-(\theta - \theta_0) \tan \phi} \quad (11)$$

with angle θ measured as indicated in Fig. 3. The shape of this failure surface is generated by a circle of varying radius

$$R = r_p \sinh[(\theta - \theta_p) \tan \phi] \quad (12)$$

rotating about an axis passing through O ; r_p and θ_p are the log-spiral radius and angle depicting the position of Point P in Fig. 3.

Line ABC marks the contour of the slope. Velocity v of soil particles within the rotating volume is a function of radius ρ and angle θ , and it is defined by equation

$$v = \rho \omega \quad (13)$$

where ω = angular velocity about O , and the velocity is perpendicular to radius ρ (Fig. 3).

The two circles beneath the slope are cross sections of the conical surface with two radial planes. The shaded sections indicate portions filled with the soil. The geometry of the mechanism is fully described by angles θ_0 and θ_h , and the ratio of radii in Eqs. (10) and (11) at $\theta = \theta_0$, i.e., r'_0/r_0 .

The kinematic approach of limit analysis is based on the balance equation of the work rate, written for an incipient failure process, with the components of the equation including the work of the soil weight and the work dissipated by the soil during failure. The work rate of the soil weight is calculated from a general expression

$$W_\gamma = \int_V v_i \gamma_i dV = \gamma \int_V v \cos \theta dV \quad (14)$$

where v_i and γ_i = velocity vector and the unit weight vector, respectively, and v and γ = magnitudes. The shape of the rotating volume V is complicated, and the details of integration are given in the Appendix.

The work dissipated by the soil during plastic shear, per unit area, is equal to $cv \cos \phi$ [see, e.g., Drucker and Prager (1952)]. Integrating this dissipation rate over the curvilinear surface $RSR'T$ (Fig. 2) with varying velocity [Eq. (13)] is an elaborate exercise; therefore, a different method is used here. This method is based on the unique relation of shear to the volumetric deformation in plastically deforming soils. Consequently, rather than calculating the work of shear along the failure surface, one can calculate the volumetric deformation in the entire mechanism, and relate the rate of work dissipation to this integrated volumetric strain rate. The total volumetric strain rate is easily calculated as an integral of the velocities over surface S bounding the mechanism. The expression for the rate of work dissipation in the mechanism then becomes

$$D = c \cot \phi \int_S n_i v_i dS \quad (15)$$

where n_i and v_i = outward unit vector normal to surface S and the velocity vector, respectively (Appendix). This method was first described in the context of 3D bearing capacity calculations (Michalowski 2001), and more recently it was adopted in 3D analysis of slopes (Michalowski and Drescher 2009). The reader will find a more comprehensive description of this method in either reference.

By equating the work rate of the soil weight in Eq. (14) to the dissipation rate in Eq. (15), the dimensionless critical height $\gamma H/c$ was calculated, and the best estimate (upper bound) of its critical value was sought using a minimization process with geometric parameters θ_0 , θ_h , and r'_0/r_0 being variable.

In searching for the minimum value of $\gamma H/c$, the mechanism in Fig. 3 was modified to a case where the upper log-spiral was located across Point O as illustrated in Fig. 4, and given in equation

$$r' = -r_0 e^{(\theta - \theta_0) \tan \phi} \quad (16)$$

This mechanism was automatically included in the optimization procedure when ratio r'_0/r_0 assumed negative values. The mechanism in Fig. 4 is generated by a rotating circle of varying diameter; this time, however, the circle is rotated about its cord passing through Point O .

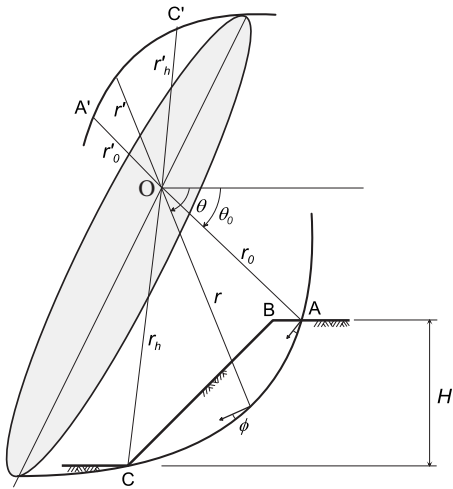


Fig. 4. 3D mechanism generated by a circle of varied diameter rotated about its cord [after Michalowski and Drescher (2009)]

Before calculations were carried out, the mechanism in Fig. 2 was modified with a plane insert as illustrated in Fig. 5. This is to assure that if no constraint is placed on the width of the failing soil mass, the collapse pattern will tend to a plane-strain mechanism. The plane portion of the mechanism was consistent with the geometry of the curvilinear parts, and the composite failure surface was smooth (see comment in the Appendix). The number of independent parameters describing the surface was then increased by only one, i.e., the relative width of the plane insert b/H .

Mechanism for Undrained Failure

The strength of soils during undrained failure is described by shear strength c_u , and the deformation of the soil is incompressible. The kinematically admissible rotational mechanism is then described by a curved cylinder (torus) rather than a curved cone. The procedure for calculations $\gamma H/c_u$ is similar to that for frictional soils, but the work dissipation rate needs to be calculated differently, because formula (15) cannot be applied when $\phi=0$. The rate of work dissipation is now calculated from

$$D = c_u \int_S v dS \quad (17)$$

with v being the magnitude of the velocity jump vector on the sliding surface S (kinematic discontinuity). A more detailed expression is given in the Appendix.

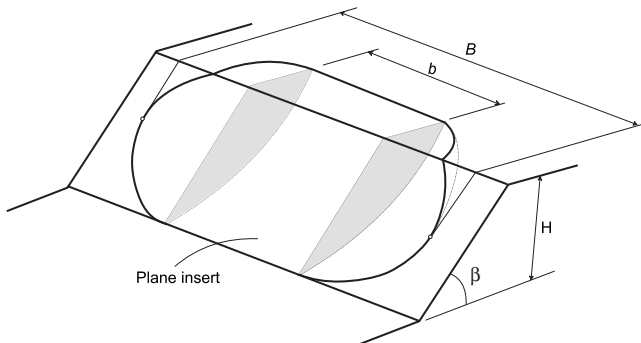


Fig. 5. Schematic of the mechanism with a plane insert

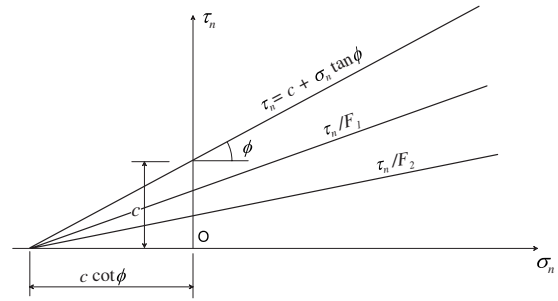


Fig. 6. Independence of parameter $c \cot \phi$ of the safety factor

3D Safety Factors for Slopes

Presentation of Stability Charts

Typical charts representing results of slope stability analyses require an iterative procedure to arrive at the safety factor. For instance, the Taylor (1937) charts are given in terms of stability factor $c_d/\gamma H = c/\gamma H F$, where c_d is the cohesion intercept needed to maintain limit equilibrium. Factor $c/\gamma H F$ is then plotted versus the slope inclination angle for a variety of internal friction angles ϕ . The safety factor is described in a manner similar to that for undrained analysis

$$F = \frac{c}{c_d} = \frac{\tan \phi}{\tan \phi_d} \quad (18)$$

For given β and ϕ one can find $c/\gamma H F$ from Taylor's charts, and, given $c/\gamma H$ for the slope, calculate F . But the safety factor needs to be applied also to $\tan \phi$; hence the process becomes iterative. There have been some attempts in the past to present the stability analysis results without the need for iterations. Of those, the method suggested by Bell (1966) is perhaps the most convenient, and it was used earlier to present the results from plane-strain limit analysis (Michalowski 2002). Iterations will not be needed if the results are plotted as a function of $c \cot \phi$. This is because $c \cot \phi$ is independent of the safety factor. This is a direct consequence of the definition in Eq. (18), and it is illustrated in Fig. 6. No matter what the safety factor, product $c \cot \phi$ remains the same. It is useful then to plot the reciprocal of $\tan \phi_d$ (or $F/\tan \phi$) versus dimensionless group $c/\gamma H \tan \phi$, and produce charts for various slope inclination angles. For 3D analysis the charts also need to describe the dependency of the safety factor on the width of the mechanism relative to the slope height.

Minimization Procedure

A computer program was written to calculate the work rate of the soil weight and the work dissipation rate during incipient slope failure. The best estimates of critical $\gamma H/c$ were obtained using a minimization procedure for given slope inclination angle and internal friction angle ϕ . Parameter $c/\gamma H \tan \phi$ was then calculated; this approach yields a rigorous lower bound to $c/\gamma H \tan \phi$. The size of the mechanism was subject to an independent constraint on its total width B , and the results are presented as a function of relative width B/H . However, the relative width b/H of the plane insert could vary, subject to the constraint on the overall mechanism width B/H . Independent variables in the minimization procedure were: angles θ_0 and θ_h , ratio r'_0/r_0 , and the relative width of the plane insert b/H . These parameters were varied by a small increment in a single computational loop, and

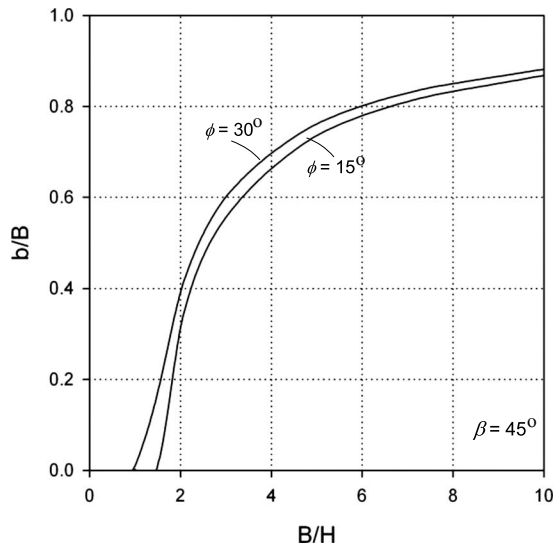


Fig. 7. Change in the relative width of the plane insert b/B as a function of the overall constraint on the width of the mechanism

the process was repeated until the minimum of $\gamma H/c$ was reached, with the increments of 0.01° used for angles θ_0 and θ_h , and 0.001 for ratio r'_0/r_0 and insert width b/H (initial increments in the procedure were set to 5° and 0.1, respectively, and were gradually reduced to 0.01° and 0.001; a typical time for calculation of a single data point on a PC with processor of 2.83 GHz was about 15 s, and it was dependent on the initial guess). For failures constrained to a narrow width (e.g., $B/H < 1.5$ for $\beta = 45^\circ$ and $\phi = 15^\circ$), the best estimate of $c/\gamma H \tan \phi$ was found for the mechanism without the plane insert. However, with an increase in the overall width of the mechanism, the width of the insert rapidly increases, as illustrated in Fig. 7 for a 1:1 slope. In all cases, the most critical mechanism reached the constraint B/H on the overall width.

Computational Results

Computational results are first presented for undrained failure, Fig. 8. Coefficient $c_u/\gamma HF$ is presented as a function of slope inclination angle for several ratios B/H . The most upper line is for the plane-strain mechanism, and its horizontal portion describes results with the mechanism increasing to a great depth (see Michalowski 2002). The use of this chart is straightforward: for a given geometry of the slope one reads $c_u/\gamma HF$, and calculates safety factor F for given (noncritical) $c_u/\gamma H$.

The remaining computational results (for soil strength characterized by ϕ and c) are presented as functions of $F/\tan \phi$ versus $c/\gamma H \tan \phi$ for widths of the failing slope B/H ranging from 1.0 to 5.0, and for the plane-strain case. Each chart illustrates results for one inclination angle of the slope. The results for slopes of inclination of 30° and 45° are shown in Fig. 9, those for 60° and 75° in Fig. 10, and Fig. 11 illustrates the results for vertical slopes. To make the comparison of this solution to other (future) solutions possible, Table 1 is included with numerical values of magnitudes of coefficient $c/\gamma H \tan \phi$ for a 1:1 slope ($\beta = 45^\circ$), as a function of $1/\tan \phi$ (i.e., $F/\tan \phi$ when $F=1$). The precision of the reported values is for comparative reasons, and it is not to suggest that all digits are practically meaningful. The last column in the table ($B/H = \infty$) is from calculations for a 2D mechanism (Michalowski 2002). Numerical values of nondimensional critical

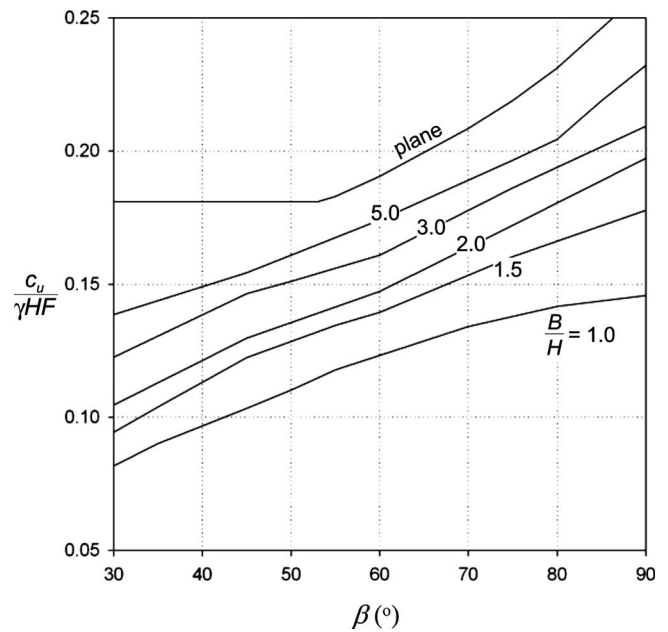


Fig. 8. Undrained slope failure: $c_u/\gamma HF$ as a function of the slope angle

height $\gamma H/c$ for 3D failures obtained using the same method, for a wide variety of parameters, can be found elsewhere (Michalowski and Drescher 2009).

It was already indicated in Fig. 7 that for slopes with relatively low constraint on width B/H (for instance, $B/H=1.5$ for $\beta=45^\circ$ and $\phi=15^\circ$), the most adverse mechanism is defined by the 3D failure surface alone. The plane insert illustrated in Fig. 5 becomes a part of the critical mechanism for wider slopes. Consequently, with an increase in B/H , the safety factor approaches the one from 2D analysis. The difference in the safety factor of slopes with different constraints of their failure mechanisms can be measured by the vertical distance between the respective lines in Figs. 8–11. Typically, once the constraint on the width of the mechanism reaches $B/H=5$, the difference between the 3D factor of safety and that from the 2D analysis is less than 10%. However, this difference can exceed 50% when the mechanism is constrained to a narrow width of $B/H=1$.

Example

A uniform 1:1 slope is built of overconsolidated soil with $\phi = 20^\circ$ and cohesion intercept $c=20$ kPa; the unit weight of the soil is $\gamma=18$ kN/m³. The height of the slope is 15 m, and its width is restrained to 30 m by rock formations. To determine the safety factor of this slope, we first calculate $c/\gamma H \tan \phi \approx 0.20$. From Fig. 9 for $\beta=45^\circ$ and $B/H=2$ one reads $F/\tan \phi = 3.25$, and $F=3.25 \tan 20^\circ = 1.18$. Plane-strain analysis yields $F=1.09$.

Significant Load on Slopes

3D failures can be triggered in slopes by strength inhomogeneities or hydraulic conditions with 3D seepage patterns, or they can occur due to geometric constraints, for instance, in the case of excavation slopes. For uniform slopes, plane-strain analyses always yield the minimum safety factor. However, a load placed on a limited area of the top surface of the slope may change this

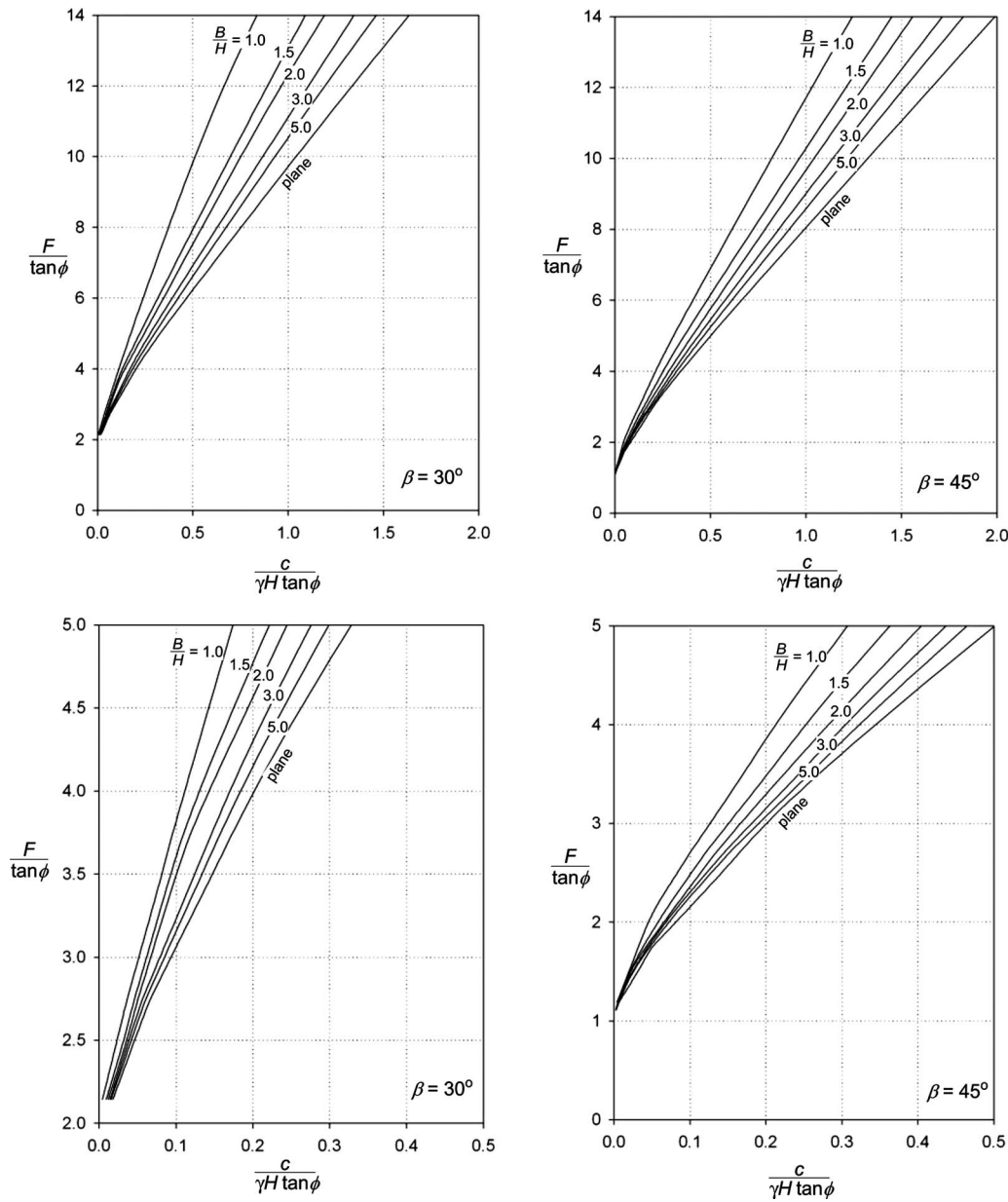


Fig. 9. 3D stability charts for slopes: $\beta=30^\circ$ and $\beta=45^\circ$

outcome. A *significant load* on the slope is defined here as the load that would change the tendency of the slope to fail from the 2D mode to a 3D type. It is useful to emphasize that, if the load distributed on a portion of the surface is small enough (less than *significant*), the 3D analysis including this load will still yield a safety factor that is larger than that from the 2D analysis with no load at all.

Considerations in this section shed some light on the magnitude of the *significant load*. This problem can be posed as follows: what is the magnitude of the load spread over a given portion of the top surface, so that a 3D safety factor for the loaded slope becomes lower than a factor from a 2D analysis with no load?

A schematic of a slope loaded on a square area $a \cdot a$ is illustrated in Fig. 12. This load can be easily accounted for in calculations by including a term due to the work rate of given load p . This term is included in the original balance Eq. (2), but was not

used in arriving at the results presented in Figs. 8–11 for load-free boundaries.

Depending on the intensity of the load and the size of the loaded area, the most critical mechanism may include the full load [Case 1 in Fig. 12(b)], or it may intersect the load (case 2). Both cases were considered when finding the best estimate (minimum) of the critical height.

If the load is small, the effect on the failure mode is negligible, and the plane-strain analysis (with no load) will yield the least safety factor. However, if the load is large, a 3D failure mechanism for loaded slope may produce a lower safety factor than the plane-strain analysis with load-free boundary does. Attention was paid to this issue in an earlier paper on 3D slope analysis (Michalowski 1989).

The outcome of calculations for a 1:1 slope and $\phi=15^\circ$ is illustrated in Fig. 13. The load is characterized by dimensionless number $p/\gamma H$, and it is spread on a square area of width a/H

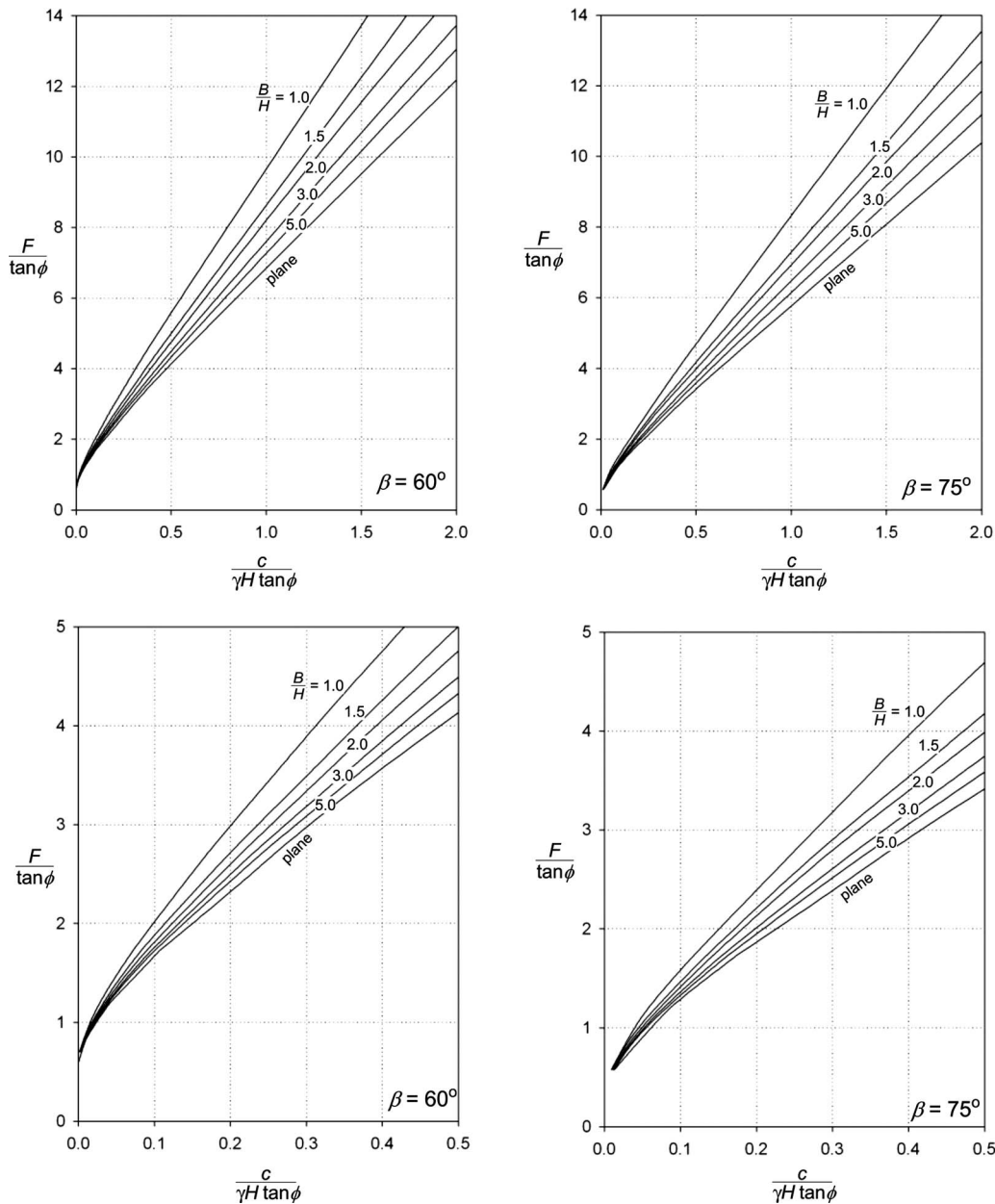


Fig. 10. 3D stability charts for slopes: $\beta=60^\circ$ and $\beta=75^\circ$

$=0.5$, as illustrated in Fig. 12. The critical height $\gamma H/c$ is plotted versus the width of the mechanism B/H . For a given slope characterized by a noncritical combination of parameters $\gamma H/c$, the curves in Fig. 13(a) are in some proportion to the safety factor (even though the plot is for one value of ϕ); i.e., for a slope of given height, an increase in critical height $\gamma H/c$ indicates an increase in the safety factor and vice versa.

The plane-strain analysis with no load on the slope surface yields the critical value $\gamma H/c=12.052$, and it is marked by a horizontal line in Fig. 13(a). When the load is relatively small, for instance $p/\gamma H=0.2$, the critical height decreases with the increase in the mechanism width, and the mechanism tends to a plane-strain failure, i.e., the plane mechanism with a loadfree boundary yields the minimum safety factor. However, if the load is increased to $p/\gamma H=0.6$, the ascending line in Fig. 13(a) indicates that a 3D failure mechanism is more critical than a 2D pattern of failure (with zero load), and the lowest critical height (and the

lowest safety factor) is produced in the analysis with the width of $B/H=1.75$. This width is now the outcome of the analysis, and not an independent constraint.

This tendency for the load to affect the outcome of the analysis is due to two competing effects. A reduction in the width of the mechanism tends to increase the safety factor (or critical height) as the shape of the failure surface becomes geometrically more restrained (less freedom to assume the least favorable geometry of failure). However, the adverse effect of the load distributed on a limited area increases with the decrease of the mechanism width. For a small load, the 3D effect dominates, and the safety factor (or critical height) decreases with the increase in the mechanism width. With an increase in load p however, it is the load that gains the dominant role, and the safety factor decreases with the decrease in the mechanism width. It is interesting to notice that one can identify a load where the two effects nearly balance out, and

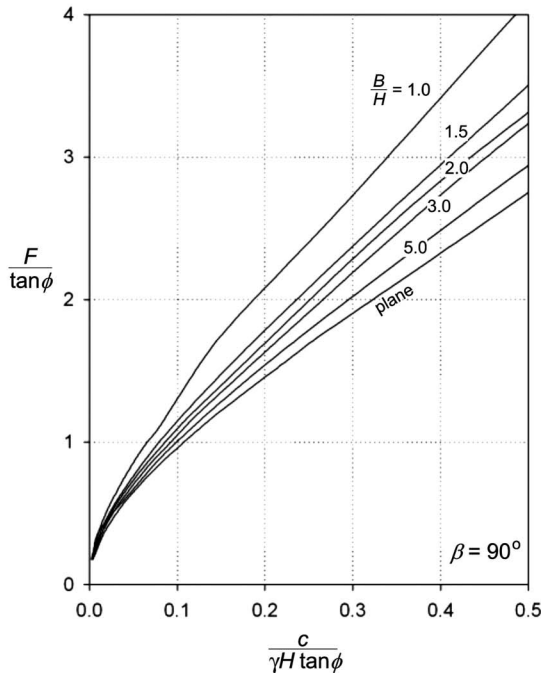
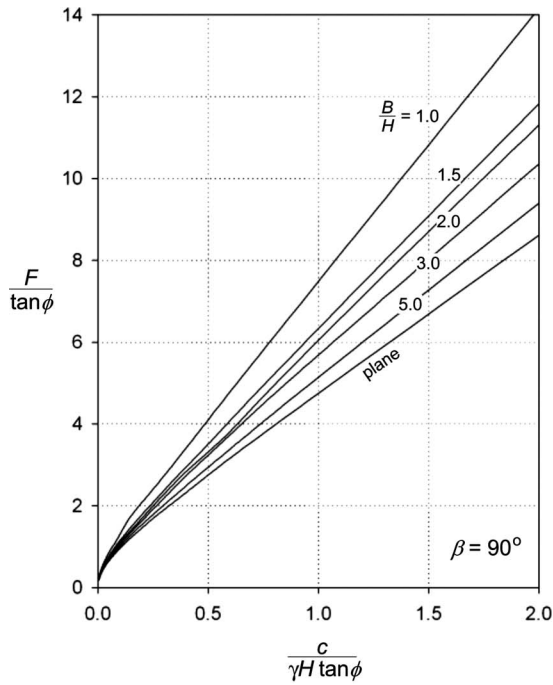


Fig. 11. 3D stability charts for vertical slopes

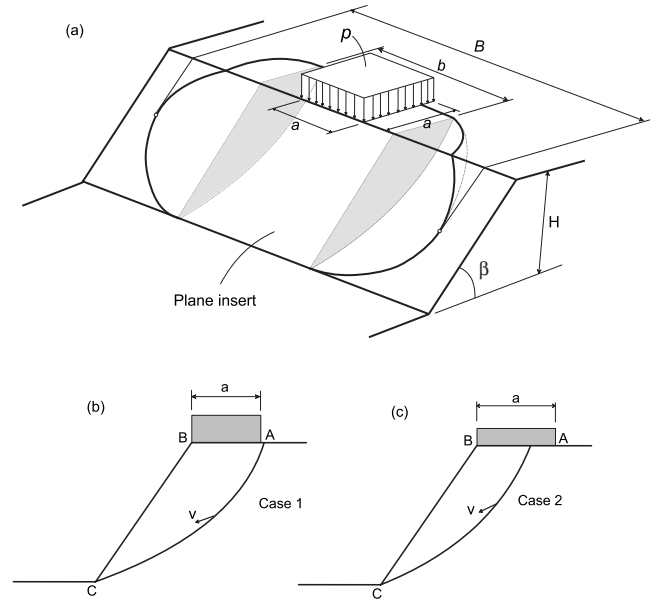


Fig. 12. Slope loaded on a square area

the critical height is independent of the mechanism width; for this example, that load is $p/\gamma H=0.35$.

The reader will notice that for width $B/H < 1.75$, the 3D effect becomes dominant for all loads, and the critical height rapidly increases. The mechanism is now “jam-packed” in a narrow space, and with the further decrease in the mechanism width an admissible toe mechanism of the type described can no longer be found. A 3D rotational failure can still occur, but not reaching the slope toe.

The “significant load” as defined in this section is shown in Fig. 13(b) as a function of the slope angle. For the 1:1 slope and with $\phi=15^\circ$, this significant load $p/\gamma H$ was equal to 0.35, and it varies between about 0.47 and 0.29 for slopes with inclination angle between 30° and 70° . This result is valid for the load on a square of $0.5H \cdot 0.5H$ at the edge of the top surface. This is a very substantial load, comparable to the weight of the soil column of a half to one-third of the slope height. This load is not to be confused with a load on a small area (such as a footing) that might produce a local bearing capacity type of failure.

Final Remarks

It has been indicated earlier for specific examples that the kinematic approach of limit analysis yields an upper bound to the

Table 1. Critical Values of $c/\gamma H \tan \phi (\times 10^2)$ for Slopes with $\beta=45^\circ$ (All Values Need to Be Multiplied by $\times 10^{-2}$)

ϕ (deg)	$\frac{1}{\tan \phi}$	B/H				
		1.0	2.0	3.0	5.0	∞
3.5	16.35	149.53	186.53	205.35	218.70	238.09
5	11.43	93.497	122.62	134.49	143.06	155.48
10	5.671	30.741	48.855	52.947	56.332	60.918
15	3.732	18.971	25.089	27.180	28.744	30.965
20	2.747	10.395	13.870	14.998	15.749	17.001
30	1.732	3.158	4.053	4.335	4.559	4.873
40	1.192	0.415	0.536	0.575	0.603	0.642

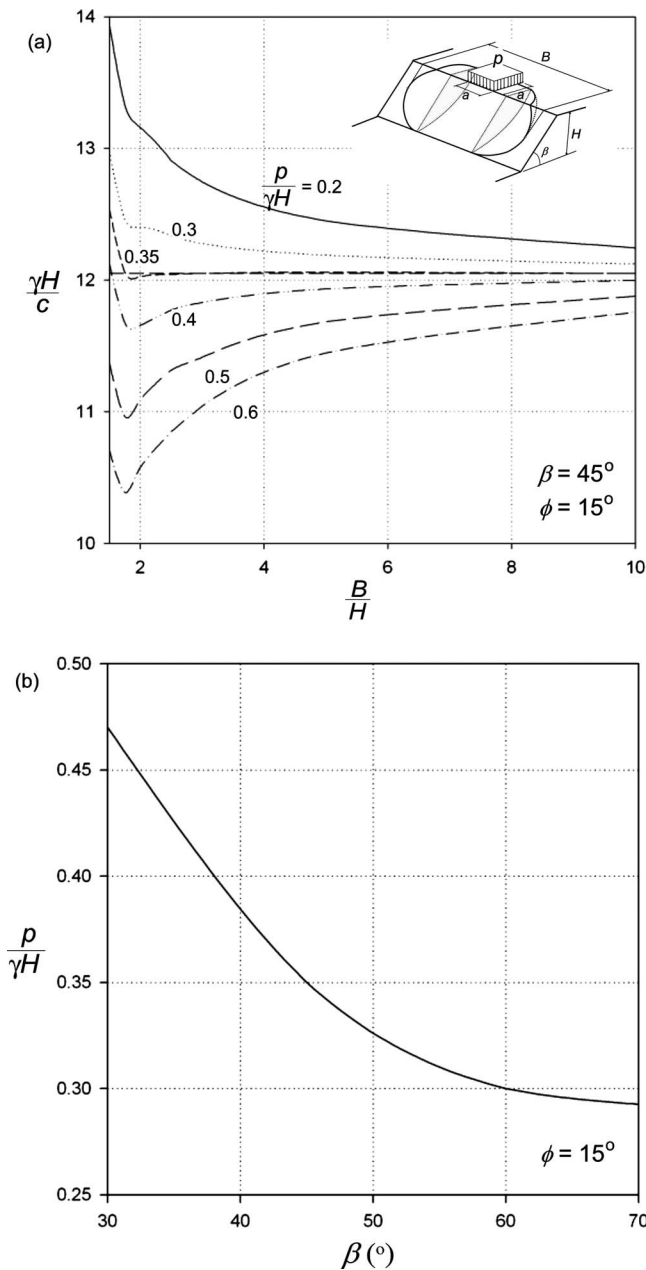


Fig. 13. 3D stability analysis of a loaded slope: (a) effect of the load on critical height of the slope; (b) significant load

critical height of the slope. This statement is now proved to be more general, and it follows that the factor of safety determined by the kinematic approach is also an upper bound on its “true” value. These statements hold true for both 2D and 3D analyses.

A tractable 3D analysis of slope stability was carried out based on a rotational failure mechanism. The failure surface has a spoonlike shape, and is a portion of a curvilinear cone surface (a “horn-type” shape). It is demonstrated that the results can be presented in the form of stability charts, which do not require an iterative procedure to arrive at the safety factor. These charts are useful where the width of the potential failure mechanism is restricted, for instance in cases of excavation slopes. Such analyses are also relevant in back calculations of soil properties from case histories with 3D slope failures. The difference in the safety factor of a slope with a failure mechanism constrained to a width equal to the slope height ($B/H=1$) and the safety factor from the

2D analysis can exceed 50%, but this difference drops down, typically to less than 10%, once the relative width of the mechanism increases to $B/H=5$.

3D failures may occur due to inhomogeneities in material properties, for instance lenses of a weaker material, or a drop in hydraulic conductivity leading to locally increased seepage. It may also occur if the slope width is physically limited, or the slope is loaded on a limited area. The latter was explored in this paper. It appears that a static load on a limited area producing the safety factor from a 3D mechanism lower than the 2D factor for a slope with load-free boundary, is quite large. For instance, for a 1:1 slope, and the load distributed on a square area $H/2 \cdot H/2$, the distributed load needs to be larger than $0.35\gamma H$ for the 3D analysis to give a safety factor lower than the 2D analysis does.

Acknowledgments

This work was carried out when the writer was supported by the Braun/Intertec Visiting Professorship at the University of Minnesota. A portion of the material is based upon work supported by the National Science Foundation under Grant No. CMMI-0724022 and the Army Research Office Grant No. W911NF-08-1-0376. This support is greatly appreciated.

Appendix

The contours of the “trumpet” (or a “horn”) in Fig. 3 are described in Eqs. (10) and (11). This shape of the trumpet is generated by a circle of varying radius R with its center described by radius r_m

$$R = \frac{r - r'}{2}, \quad r_m = \frac{r + r'}{2} \quad (19)$$

A local coordinate system x, y in each radial cross section is now introduced, as shown in Fig. 3 (x perpendicular to the plane of the figure). The velocity in Eq. (13) during rotation about Point O is now expressed as

$$v = (r_m + y)\omega \quad (20)$$

where ω = angular velocity about O. The infinitesimal volume element is

$$dV = dx dy (r_m + y) d\theta \quad (21)$$

and the work rate of the soil weight in Eq. (14) now can be written as

$$W_\gamma = 2\omega\gamma \left[\int_{\theta_0}^{\theta_B} \int_0^{x^*} \int_a^{y^*} (r_m + y)^2 \cos \theta dy dx d\theta + \int_{\theta_B}^{\theta_0} \int_0^{x^*} \int_d^{y^*} (r_m + y)^2 \cos \theta dy dx d\theta \right] \quad (22)$$

The two integrals in Eq. (22) include the work of the soil weight in two portions of the rotating volume separated by the plane perpendicular to the plane of Fig. 3 and passing through Points O and B. Angle θ_B defining this plane was found from the geometrical relations in Fig. 3

$$\theta_B = \arctan \frac{\sin \theta_0}{\cos \theta_0 - A}$$

$$A = \frac{\sin(\theta_h - \theta_0)}{\sin \theta_h} - \frac{e^{(\theta_h - \theta_0)\tan \phi} \sin \theta_h - \sin \theta_0}{\sin \theta_h \sin \beta} \sin(\theta_h + \beta) \quad (23)$$

The upper integration limit on y is a function of x : $\gamma^* = \sqrt{R^2 - x^2}$, and the limits on x are $x^* = \sqrt{R^2 - a^2}$ and $x^* = \sqrt{R^2 - d^2}$ in the first and the second integral, respectively, and a and d are given in

$$a = \frac{\sin \theta_0}{\sin \theta} r_0 - r_m, \quad d = \frac{\sin(\beta + \theta_h)}{\sin(\beta + \theta)} r_0 e^{(\theta_h - \theta_0)\tan \phi} - r_m \quad (24)$$

The work dissipation rate in Eq. (15) can be more specifically written as the sum of the integrals on the boundaries with the trace AB and BC (Fig. 3)

$$\frac{D}{c \cot \phi} = 2\omega r_0^2 \left[\sin^2 \theta_0 \int_{\theta_0}^{\theta_B} \frac{\cos \theta}{\sin^3 \theta} \sqrt{R^2 - a^2} d\theta + e^{2(\theta_h - \theta_0)\tan \phi} \sin^2(\theta_h + \beta) \int_{\theta_B}^{\theta_h} \frac{\cos(\theta + \beta)}{\sin^3(\theta + \beta)} \sqrt{R^2 - d^2} d\theta \right] \quad (25)$$

Eq. (25) cannot be used for the case $\phi=0$, and for undrained cases the dissipation was calculated from the following equation

$$D = 2\omega c_u R \left[\int_{\theta_0}^{\theta_B} \int_a^R (r_m + y)^2 dy d\theta + \int_{\theta_B}^{\theta_h} \int_d^R (r_m + y)^2 dy d\theta \right] \quad (26)$$

where radius $R = \text{constant}$.

The plane insert illustrated in Fig. 5 was included with its geometry matching the 3D portions, so that the composite surface was smooth. Equations necessary to calculate the work rate of the soil weight and the internal work for the plane section can be found elsewhere (e.g., Chen 1975). The compatibility of the composite mechanism requires that angles θ_0 and θ_h are selected identical for the 2D and the 3D portions of the sliding surface.

References

- Baligh, M. M., and Azzouz, A. S. (1975). "End effects on stability of cohesive slopes." *J. Geotech. Engrg. Div.*, 101(GT11), 1105–1117.
- Bell, J. M. (1966). "Dimensionless parameters for homogeneous earth slopes." *J. Soil Mech. and Found. Div.*, 92(5), 51–65.
- Cavounidis, S. (1987). "On the ratio of factors of safety in slope stability analyses." *Geotechnique*, 37(2), 207–210.
- Chen, W. F. (1975). *Limit analysis and soil plasticity*, Elsevier Science, Amsterdam.
- Cornforth, D. H. (2005). *Landslides in practice: Investigation, analysis, and remedial/preventative options in soils*, Wiley, Hoboken, N.J.
- de Buhan, P., and Garnier, D. (1998). "Three dimensional bearing capacity analysis of a foundation near a slope." *Soils Found.*, 38(3), 153–163.
- Drescher, A. (1983). "Limit plasticity approach to piping in bins." *J. Appl. Mech.*, 50, 549–553.
- Drucker, D. C., and Prager, W. (1952). "Soil mechanics and plastic analysis or limit design." *Q. Appl. Math.*, 10(2), 157–165.
- Drucker, D. C., Prager, W., and Greenberg, H. J. (1952). "Extended limit design theorems for continuous media." *Q. Appl. Math.*, 9(4), 381–389.
- Duncan, J. M. (1996). "State-of-the-art: Limit equilibrium and finite element analysis of slopes." *J. Geotech. Eng.*, 122(7), 577–596.
- Gens, A., Hutchinson, J. N., and Cavounidis, S. (1988). "Three-dimensional analysis of slides in cohesive soils." *Geotechnique*, 38(1), 1–23.
- Griffiths, D. V., and Marquez, R. M. (2007). "Three-dimensional slope stability analysis by elasto-plastic finite elements." *Geotechnique*, 57(6), 537–546.
- Leshchinsky, D., and Baker, R. (1986). "Three-dimensional slope stability: End effects." *Soils Found.*, 26(4), 98–110.
- Michalowski, R. L. (1989). "Three-dimensional analysis of locally loaded slopes." *Geotechnique*, 39(1), 27–38.
- Michalowski, R. L. (2001). "Upper-bound load estimates on square and rectangular footings." *Geotechnique*, 51(9), 787–798.
- Michalowski, R. L. (2002). "Stability charts for uniform slopes." *J. Geotech. Geoenviron. Eng.*, 128(4), 351–355.
- Michalowski, R. L., and Drescher, A. (2009). "Three-dimensional stability of slopes and excavations." *Geotechnique*, 59(10), 839–850.
- Salençon, J. (1990). "An introduction to the yield design theory and its applications to soil mechanics." *Eur. J. Mech. A/Solids*, 9(5), 477–500.
- Taylor, D. W. (1937). "Stability of earth slopes." *J. Boston Soc. Civ. Eng.*, 24(3), 337–386.